Gravitational variation through magnetic fields for particles in fluids

Facundo Cabrera-Booman,[1] Nicolas Plihon,[2] Raúl Bayoán Cal,[1] and Mickaël Bourgoin[2]

[1] *Department of Mechanical and Materials Engineering,*
Portland State University, Portland, Oregon, USA.
[2] *Univ Lyon, ENS de Lyon, Univ Lyon 1, CNRS,*
Laboratoire de Physique, F-69342 Lyon, France.

A magnetic field (MF) is generated to modify gravity in a laboratory. The MF produces a vertical force that counteracts the gravitational field on a magnetic sphere. The perpendicular spin of particles is blocked, thus allowing spin solely around the direction of the MF. The settling of spherical magnets in a quiescent flow with a particle density of 8200 kg/m^3 and Galileo number (Ga) in the range $[100, 280]$ was studied experimentally. The results obtained by varying Ga via gravity modification to those obtained with non-magnetic spheres where Ga is modified by varying viscosity are compared. Findings showed that there is no significant difference in the trajectory angle between magnetic and non-magnetic cases, suggesting that the method for compensating gravity does not produce any spurious effect and that particle spinning has no significant effect on this aspect of the dynamics. Subtle differences in trajectory planarity were observed hinting at a possible dependence on particle spin. Results prove the validity of the method introduced here to change the gravitational strength on particles in fluids.

I. INTRODUCTION

It is of the utmost difficulty to reduce or suppress the effect of gravity in a laboratory on Earth. In the context of particle-laden flows research, only a handful of very particular situations allow it, such as the use of neutrally buoyant particles. This prevents the exploration of crucial particle/fluid mechanisms including notably inertial effects, which are intimately related to particle-to-fluid density ratio. Therefore, the means available to do experimental research in a low gravity environment while preserving the capacity to explore inertial effects due to density contrast are expensive, scarce and lack repeatability. The only options are drop towers, parabolic flights, or space experiments in the International Space Station[1–4]. In this article we present a method to compensate the gravity acting on a particle in a flow by the application of a magnetic induction. With this purpose, we revisit as a proof of concept, the problem of the settling of spherical particles in a quiescent fluid[5–10], when magnetically varying the effective gravity experienced by the particles. Relevant research on tangential topics is present in the literature of which a brief summary follows.

The focus of using magnetic fields for gravity compensation purposes has been mostly on diamagnetic objects, e.g. DNA, water or proteins. For instance, when ways to circumvent Earnshaw's theorem came to light[11,12], it was possible to levitate living diamagnetic objects such as frogs[13]. These studies were central for the technique of high-gradient magnetic separation that allows the sorting of sample components with different magnetic susceptibilities[14–16]. In parallel, the Magnetic Resonance Imaging Community developed the technical aspects to achieve an arbitrary magnetic field profile in a laboratory (or a hospital) with the use of coils[17,18]. These are apart from the study of particles in conductive fluids under the influence of external magnetic inductions, that

are central to a number of industrial situations, for instance clean metal production[19]. On the other hand, the profiles of the external magnetic induction needed to obtain a constant vertical force that can counteract gravity in a number of scenarios such as, for example, liquid helium or oxygen were also studied[20–23]. With all these tools in hand, some progress has also been made in the particular situations that interest this work: paramagnetic/ferromagnetic or permanently magnetised particles in a weak diamagnetic liquid (i.e. water), subjected to a *weak* external magnetic induction environment (thus no liquid magnetisation occurs). Some studies explored the effects of a homogeneous magnetic induction on one or more particles in non-magnetic fluids[24–28]. In these studies, the main focus was exploring the role of particle/particle interactions on their coupling with the fluid, using a homogeneous magnetic field as a way to tune interactions between particles.

In the present study the aim is to disentangle the role of particle inertia and gravity on particle coupling with the surrounding fluid. This requires modification of the settling properties of the particles independent of the inertial couplings with the fluid. This question is particularly crucial for unveiling the mechanisms at play during turbulent transport of inertial particles[29], where inertial effects (such as dynamic filtering[30] and preferential concentration[31,32]) generally parameterized by the particles' Stokes number $St = \tau_p/\tau_\eta$ (with τ_p the particle viscous relaxation time and τ_η the turbulence dissipation time) interplay with particle settling. These effects can, for instance, be parameterized by the Rouse number $Ro = \tau_p g/u_{\mathrm{rms}}$, where g is the acceleration of gravity and u_{rms} the turbulent fluctuating velocity. Exploring the role of inertia in experiments by varying the Stokes number at fixed turbulent conditions (*i.e.* for fixed τ_η and u_{rms}) requires variation of the particles' relaxation time τ_p, hence inevitably changing at the same time their Rouse number and their settling properties.

Being able to experimentally modify the effective gravity experienced by the particles would give a unique and simple way to truly explore Rouse number effects at fixed Stokes number and reciprocally. Guided by this final motivation in the context of particle laden turbulent flows, the present study first addresses, as a proof of concept of the relevance of magnetic compensation of gravity, the case of particles settling in a quiescent flow.

The rich dynamics of single spheres settling in quiescent flows has been extensively explored in previous studies[5–10,33], in particular the transitions between different settling regimes that depend on the relative importance of gravity and viscous effects (parameterized by the Galileo number) have been determined. This problem offers an appealing framework to validate the magnetic method to compensate gravity and revisit numerical simulation predictions[8,34,35] as well as previous experimental results in the literature[6,9,10,36] with an alternative method to explore the parameters space.

The problem of a single sphere settling in a quiescent viscous fluid is controlled by two adimensional parameters[9,10]: particle-to-fluid density ratio Γ and Galileo number $Ga = U_g d_p/\nu = \sqrt{|\Gamma - 1|g d_p} d_p/\nu$, with U_g the buoyancy velocity, d_p the particle diameter, g the local acceleration of gravity and ν the kinematic viscosity. As a result of numerical and experimental efforts[8,9,33] a detailed Γ – Ga map has been devised showing the different regimes that a single sphere settling in a quiescent flow undergoes. The trajectory dynamics are characterized by trajectory angle and planarity, leading to five main regimes: Rectilinear; Steady Oblique; Oblique Oscillating; Planar or Rotating; and Chaotic.

In the context of this paper, the experiments previously carried out by our group[9,10] are of particular interest as those are the only reported experiments with particle densities comparable to the magnetic particles used here. The experiments performed in this article introduce and validate an experimental technique that, making use of magnetic forces, allows modification of the effective gravitational pull on a magnetic sphere, thus changing Galileo number (recall that it depends on the local acceleration of gravity g) while keeping all other physical parameters of the problem unchanged. Moreover, as an additional effect of the magnetic field, the particle dynamics with blocked spin are studied experimentally for the first time and allows the experimental probing of the numerical prediction that particle spin should not affect the path instability dynamics[37].

The development of such an experimental method to compensate gravity provides a unique and low-cost way to study problems that were previously reserved to numerical studies: where changing the value of gravity is trivial, but where models for particle/fluid couplings, in particular in the turbulent case, are still a matter of active research. On the other hand, the experimental validation of results in numerical simulations about the influence of particle spin, previously very hard to falsify, are here validated.

The article is organized as follows. We first present the basic theoretical layout of the magnetic gravity compensation method and experimental design in Section II. The results of the sedimentation of magnetic particles with a modified gravity are described in Section III. Then, we discuss conclusions and perspectives of this work in Section IV. Finally, the Appendix presents further details on the theoretical foundation of the method, its validation, and further experimental details.

II. MAGNETIC FIELD GRAVITY CONTROL

A. General Principles

The magnetic torque ($\mathbf{T}^M$) and force ($\mathbf{F}^M$) acting on a particle with a magnetic dipole $\mathbf{M}$ and mass m in vacuum and in the presence of an external magnetic induction $\mathbf{B}$ and gravity $g\hat{\mathbf{z}}$, expressed in cylindrical coordinates, read:

$$\mathbf{F}^M = \nabla(\mathbf{M} \cdot \mathbf{B}), \qquad (1)$$

$$\mathbf{T}^M = -\mathbf{M} \times \mathbf{B}. \qquad (2)$$

Note that the magnetic torque $\mathbf{T}^M$ is restorative, i.e. $\mathbf{M}$ parallel to $\mathbf{B}$ is the stable orientation. Therefore, the particle can only freely rotate around the direction of the magnetic induction $\mathbf{B}$. Considering an external magnetic induction in the direction of gravity ($\hat{\mathbf{z}}$) an effective gravity $\tilde{g}$ can be defined and the particle equation of motion then reads:

$$\mathbf{F} \cdot \hat{\mathbf{z}} = m\tilde{g} = m[g - \mathrm{M}\nabla_z(\mathrm{B})\cos(\psi)/m], \qquad (3)$$

where $B = |\mathbf{B}|$, ψ is the angle between the vectors $\mathbf{B}$ (fixed, external magnetic induction) and $\mathbf{M}$ (free, particle orientation). Note that ψ is a constant equal to zero if there is no torque besides $\mathbf{T}^M$.

It is detailed in Appendix B 1 that in order to optimally compensate gravity a linear magnetic field is required:

$$\mathbf{B}(r, z) = (-G_z/2\ r)\ \hat{\mathbf{r}} + (G_z\ z + B_0)\ \hat{\mathbf{z}}. \qquad (4)$$

It should be noted that because of the divergence-free nature of magnetic fields, the requirement of imposing a vertical magnetic gradient to compensate gravity requires the applied magnetic field to have a radial component (first term in the l.h.s. of Eq. (4)). This radial magnetic component may induce an undesired radial drift of the particle. Applying an additional vertical offset $B_0\hat{z}$ to the applied magnetic field allows control of the relative intensity of the radial force and certainty that it is negligible with respect to other relevant forces of the problem (see below). As an additional effect, the vertical magnetic offset also allows to fix and vertically orient the particle's magnetic moment, hence only allowing particles to rotate around the vertical.

These two effects (importance of the radial magnetic force and magnetic torque) can be quantitatively estimated. Given the expression of the desired magnetic field given by Eq. (4), the order of magnitude of the magnetic-to-hydrodynamical radial force and torque reads (see Appendix B 1 for complete derivation):

$$F_r^M / F^{\text{fluid}} = \frac{|\mathbf{M}| \frac{r \ (\text{G}_z)^2/4}{\sqrt{(\text{G}_z)^2/4r^2 + (\text{G}_z z + B_0)^2}}}{1/8 C_D d_p^2 \pi \rho_f v^2} \approx \frac{10^{-6} \text{ N m}}{10^{-3} \text{ N m}} = 10^{-3},$$
(5)

$$T^M / T^{\text{fluid}} = \frac{|\mathbf{M}||\mathbf{B}|}{1/64 C_\omega d_p^5 \pi \rho_f \omega^2} \approx \frac{10^{-3} \text{ N m}}{10^{-13} \text{ N m}} = 10^{11}.$$
(6)

These values are obtained using typical values explored in this work: radial distance to axis $r = 10$ cm; axial distance to tank geometrical center $z = 10$ cm; magnetic field gradient $G_z = 290$ G/m; vertical magnetic field offset at tank geometrical center $B_0 = 20$ G; $C_D = 1$; particle diameter $d_p = 1$ mm; fluid density $\rho_f = 10^3$ kg/m^3; $v = 1$ m/s; particle angular velocity $\omega = 2$ rad/s; and rotational drag coefficient $C_\omega = 1$. Relation 5 shows that in typical operating conditions, the radial force is 3 orders of magnitude smaller than the hydrodynamical forces. Hence, no significant spurious radial drift induced by the applied magnetic field is expected. The radial magnetic force can however become significant if the applied magnetic gradient becomes too large. This will set the smaller effective gravity that can be achieved with this experimental setup without resulting in particle drift: $\tilde{g} = 0.43$ m/s^2 in the current experimental setup. In that case the typical ratio F_r^M / F^{fluid} is equal to 1.1, where a typical value $G_z = 476$ G/m was used. Therefore, when the radial magnetic force and the fluid force become comparable, drift occurs.

On the other hand, relation B7 justifies the claim that the angle ψ between the particle magnetic moment $\mathbf{M}$ and $\mathbf{B}$ can be taken as approximately zero. The magnetic torque is orders of magnitude larger than the hydrodynamic torque, hence the particle can only rotate about the magnetic field direction that is set as the vertical (see Eq. 2).

B. Experimental Setup

The experiments are performed in a transparent PMMA water tank with a square cross-section of 170×170 mm^2 and a height of 710 mm, shown in Fig. 1. The tank is filled with different mixtures of pure glycerol (Sigma-Aldrich W252506-25KG-K) and distilled water, ranging from 0% to 40% glycerol concentration. Viscosity is measured with a rheometer Kinexus ultra+ from Malvern industries with a maximum uncertainty of 0.6%. The kinematic viscosity ν ranges from 10^{-6} to 1.05×10^{-3} m^2/s. Furthermore, an air-conditioning system keeps a constant room temperature of $(22 \pm 0.6)^\circ$C
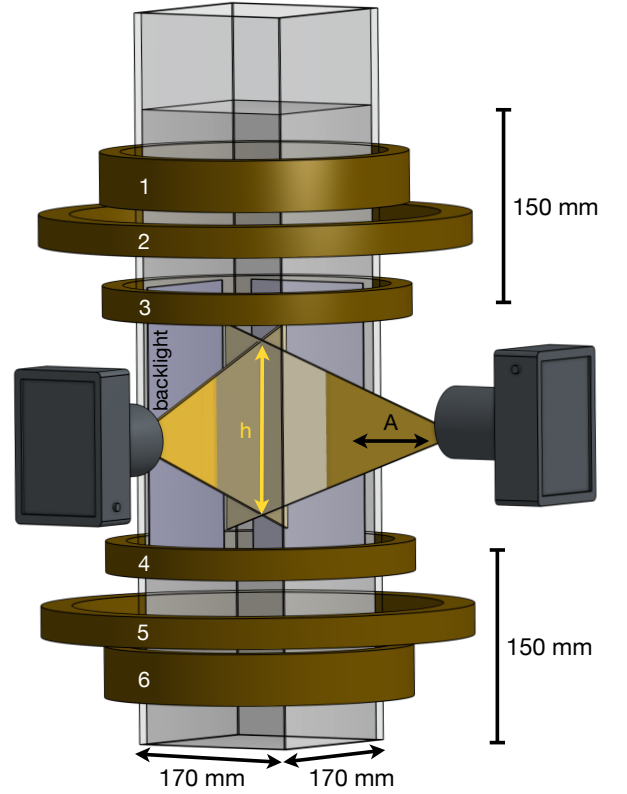

FIG. 1. Experimental setup. Two cameras image the particles inside the water tank. Six circular coils produce a magnetic induction used to compensate gravity on magnetic particles.

yielding a 2% uncertainty on the precise value of the viscosity.

A 150 mm region of fluid above and below the visualization volume is set to ensure both the disappearance of any initial condition imposed on the particles when released and the effects of the bottom of the tank. Furthermore, a minimum distance of 20 mm between the tank walls and the particles is maintained. In this configuration and using correlations available[38], the settling velocity hindering due to wall effects is estimated to be lower than 3%, thus neglected.

To record the trajectory of the particles, two high-speed cameras (model fps1000 from The Slow Motion Company) image the water tank with a resolution of 720×1280 px^2 and 2300 fps. These dual recordings allow the implementation of a 4D-LPT (Lagrangian Particle Tracking resolved in time and in three dimensions)[39]. This method accurately tracks particles with a precision of approximately 90μm. This level of precision is determined by assessing the disparity between rays during the stereo-matching process between the two cameras. It is important to note that the experimental noise affecting particle position is short-term in nature. However, this noise is effectively mitigated due to the temporal redundancy achieved through oversampling at a high frame rate of 2300Hz. Additionally, Gaussian filtering is ap-

TABLE I. Characteristics of the coils used for the magnetic compensation of gravity. Columns show the following parameters for each coil used: number of turns N, radius R, and cross section σ. Each coil is represented by a number as in Fig. 1.

	1	2	3	4	5	6
N	965	103	450	452	101	969
R (cm)	16.3	22.1	15.6	15.4	21.8	16.1
σ (cm^2)	15.6	3.9	3.6	3.6	3.9	15.6

plied to the trajectories, further enhancing the accuracy of particle velocity estimation. Consequently, the uncertainty associated with instantaneous velocity along these trajectories is less than 4 mm/s[39]. Moreover, when the velocity is averaged over a specific trajectory, the associated uncertainty of the mean velocity estimate decreases to within a few hundred microns per second.

Backlight illumination is used, as represented by the dark blue rectangles in Fig. 1. The distance A from the cameras to the exterior of the tank's wall was varied in order to change the extent of the tracking region, which impacts the tracking resolution. However, for consistency between datasets, the measurement volume was restricted at a value of $h \times 100 \times 100$ mm^3 by cropping the images.

The particles used here are spherical permanent neodymium magnets with: mass density $\rho_p = 8200$ kg/m^3; diameter $d_p = 1$ mm; and average arithmetic roughness $Ra = 15$. The surface roughness of particles has been proved to influence the boundary layer, therefore modifying several aspects of the dynamics[40–42]. Note that the values of $Ra/d_p < 5 \times 10^{-2}$ mm^{-1} obtained are small and not expected to considerably modify the dynamics[41]. Therefore, the ranges of adimensional numbers reached are Ga = [100, 280] and Γ = [6.8, 8.2]. Furthermore, the magnetic moment $|\mathbf{M}|$ is computed using Equation C1 yielding $|\mathbf{M}| = 4.96 \times 10^{-4}$ Am^2. Particle dimensions and shapes were measured using a microscope with a precision of 10 μm. In particular, no significant deviation from the spherical shape or the documented diameter could be measured. Particle mass is measured with a precision of 1×10^{-3} g via a standard laboratory scale. The surface roughness of the particles was measured with a Scanning Electron Microscope (SEM) model ZEISS SUPRA 55 VP, over an area of 200×500 μm^2, and quantified by the average arithmetic roughness Ra.

To produce the external magnetic induction, a six-coil system has been put in place, as represented in Fig. 1. They are placed at vertical distances Z_i ($i \in [1, 6]$) from the origin of coordinates, set at the middle distance between coils 1 and 6. The position of the coils and electrical current input in order to produce either a magnetic induction or its gradient as homogeneous as possible within the measurement volume was estimated based on the numerical computation of the corresponding magneto-static

equations (see Sec. II A). To simplify computations each coil was modelled as an infinitesimal current loop. The effective number of turns and radius of the current loop that models each finite size coil is experimentally determined in the following manner. Knowing the current input, the axial ($r = 0$ in cylindrical coordinates) magnetic induction as a function of the distance to the coil geometric center is measured for each coil using a Teslameter Bell 7030. Later, the effective number of turns and radius are obtained via a non-linear fit of the measurements to the theoretical axial magnetic induction of a current loop of infinitesimal size:

$$B(z) = 2\pi 10^{-7} \frac{R^2 N I}{(z^2 + R^2)^{3/2}}, \qquad (7)$$

with N the effective number of turns; R the coil radius; I the current; and z the distance from the coil individual geometric center.

The coils' effective parameters are presented in Table I. The uncertainty on N and R by the aforementioned method are estimated to be 4% and 3%, respectively, while the coils' cross-section (σ) uncertainty is 0.4 cm^2.

C. Magnetic Field Production

The six circular coaxial coils used to generate the required magnetic induction (Eq. 4) are sketched in Fig. 1, and their characteristics were shown in Table I. The coils are modelled as infinitesimal current loops, therefore the theoretical axial magnetic induction at the six-coil system axis reads:

$$\mathbf{B} \cdot \hat{\mathbf{z}} = 2\pi 10^{-7} \sum_{i=1}^{6} \frac{R_i^2 \, N_i \, I_i}{((z + Z_i)^2 + R_i^2)^{1.5}}. \qquad (8)$$

In order to set the magnetic field presented in Eq. 4 at the laboratory, a nonlinear least squares fit of Eq. 8 to the axial component of Equation 4: $B_z = G_z \, z + B_0$ is performed. The fit's fixed parameters are: N_i; R_i (coil's radius); G_z; B_0; and Z_{fit} the range at which the fit is performed. The outputs are: I_i the current in each coil; and Z_i the distance between the coils geometrical center and the origin of coordinates $z = 0$ (located at the geometrical center of the coils).

Note that there is no radial dependence on Eq. 8. The magnetic field outside the axis is estimated by Maxwells' equations, i.e. the inhomogeneity deduced theoretically in Appendix B 1 (see Fig. 7) is used to estimate the magnetic field out of the axis. The magnetic induction homogeneity outside the axis was measured with a Teslameter and it was found to be accurately represented by Fig. 7.

Two sets of values for G_z, B_0 and Z_{fit} were chosen:

1. **Case g_0: homogeneous vertical magnetic induction.**

TABLE II. Details of the two external magnetic inductions implemented here: Case g_0 and g^*.

	Non-linear fits		Measurements	
	Case g_0	Case g^*	Case g_0	Case g^*
G_z (G/m)	0	-290	0 ± 20	-286 ± 25
B_0 (G)	20	26	20 ± 1	22 ± 1
Z_{fit} (mm)	(-150, 50)	(-100, 0)	✗	✗

In this case $\nabla_z B = 0$ & $B \neq 0$, yielding no net magnetic force and only impacting the particles' rotation through the blocking effect of the magnetic torque previously discussed.

2. **Case g^*: constant gradient vertical magnetic induction.**
   In this case $\nabla_z B \neq 0$ & $B \neq 0$, yielding both a net magnetic force (used to compensate gravity) and a net magnetic torque, resulting in the rotation-blocking effect, respectively.

The two cases differ on the magnetic force magnitude (proportional to $\nabla_z B$) that they impose on the particles: whereas the Case g^* blocks the rotation and applies a force, Case g_0 blocks the rotation but the applied force is negligible. In particular, the size of the fit window Z_{fit} needed to be shortened for Case g^*, to minimise inhomogeneities in the magnetic force. The specific values of these two sets of input parameters in the non-linear fit to Eq. 8 are presented in Table II, which are with the corresponding magnetic induction measurements discussed below. Details about coils' parameters for both cases are detailed in Appendix A.

Fig. 2 presents the profiles of axial magnetic induction B_z (first row) and its gradient $\nabla_z B$ (second row) obtained from the non-linear fit (black lines), and measurements performed with a Teslameter Bell 7030 (blue crosses), versus distance to the origin. Finally, the blue shade represents the region (Z_{fit}) where the fit was performed. Note that because the magnetic field is measured at the axis, and the equation fitted represents the center of a current loop (where the magnetic field is purely vertical): $\mathbf{B} = B_z \hat{\mathbf{z}}$.

It can be seen that, for Case g_0, the magnetic induction measurements (Fig. 2(a)) overlap with the simulations, whereas the magnetic induction gradient (Fig. 2(c)) presents an average difference of 10%, with maximum values of 30% that occur near the extremes of Z_{fit}. On the other hand, Case g^* has a 10% discrepancy on the magnetic induction gradient $\nabla_z B$ (Fig. 2(d)), while the magnetic field overlaps with the measurements in the range $Z_{fit} \in (-0.1, 0)$ m (Fig. 2(b)). Additionally, note that the radial-to-axial force ratio (Equation B5) takes the following maximum values for Cases g_0 and g^*: 1×10^{-2} and 1.5×10^{-1}, respectively.

In the case of the 1 mm spherical permanent magnets that are studied here, these inhomogeneities in the magnetic induction gradient produce a 5% variability in the
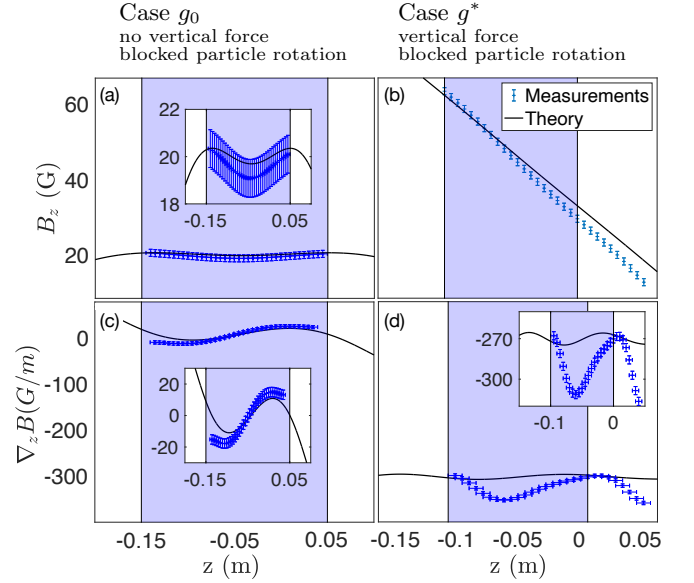

FIG. 2. Gradient of B_z computed from the axial magnetic induction measurements (blue points) and simulations (black line). The insets present the measurements and simulation results of the axial magnetic induction as a function of the distance to the origin z=0. Finally, a horizontal arrow denotes the rightwards gravity direction.

effective gravity value for Case g^*, and an effective gravity between $\tilde{g} = 9.5$ m s^{-2} and 9.8 m s^{-2} for Case g_0.

The presence of oscillations in the magnetic field can be explained as the interference between the higher harmonics that compose the total magnetic induction of each coil, as observed in the literature[20]. The interaction between these higher harmonics can be modified considerably by small errors in the coil positioning. To explore this idea Fig. 3 shows the theoretical magnetic induction (a) and gradient (b) for Case g^*, evaluated at different Coil 1 positions Z_1: its original position (black); 5 mm downwards (red); and 5 mm upwards (magenta). While the magnetic inductions are indistinguishable (Fig. 3 (a)), the gradients show clear differences (Fig. 3 (b)): within the measurement region (blue shade) a difference of up to 3% is present. Note that the coil positioning error is estimated to be 5 mm, this value includes the approximation of the coils by an infinitesimal loop at its geometrical centre and the 2 mm precision in positioning due to the tools used. These factors are hypothesized to produce the difference between the experimental measurements and the simulated values encountered in Fig. 2.

D. Data Sets

The camera-tank distance A was varied to obtain two different measurement volume heights h (see Fig. 1): $h = 100$ mm and $h = 200$ mm. This translates into different maximum particle dimensionless trajectory lengths
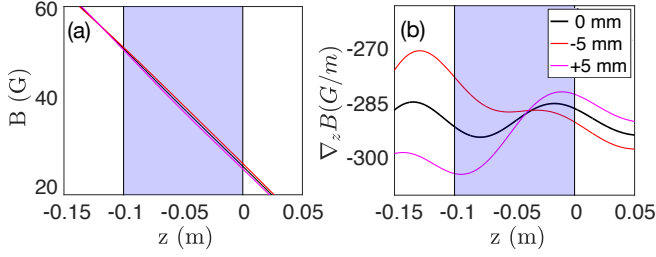
FIG. 3. Theoretical magnetic field (a) and gradient (b) for Case g^*, evaluated at different coil Z_1 positions. The original coil position (black); 5 mm downwards (red); and 5 mm upwards (magenta) are shown.

$l^*_{max} = h/d_p = 100$ & 200 (recall that d_p is 1 mm for all cases), while the measured volume has a 150×150 mm^2 transverse section. In order to reduce experimental noise (due to inevitable particle detection errors in the Lagrangian particle tracking treatment[43]), the raw trajectories are smoothed by convolution with a Gaussian kernel of width $\sigma = 12$ frames; acting as a low-pass filter with a cut-off frequency $f_c = \text{fps}/\sigma = 2300$ Hz$/\sigma = 192$ Hz. Quantities in this report are non-dimensionalized (denoted by a superscript asterisk, for instance U^*) by the following time, length and velocity scales: d_p/U_g; d_p; and U_g, respectively.

The experimental procedure is as follows: Initially, the tank is filled with a water-glycerol mixture, and approximately 24 hours are allowed to pass. During this time, the temperature at various locations within the bulk of the fluid stabilizes to within a temperature difference of less than $0.6°C$. Subsequently, a standard calibration process for the 4D-LPT system is executed[39]. Once calibration is complete, the magnetic field is activated, and spherical particles are released from a 0.5cm-diameter plastic tube positioned at the center of the tank, approximately 5cm above the region of interest (ROI). The particles are carefully introduced one by one into the tube, where they settle due to gravitational forces. To ensure that the fluid remains undisturbed between successive particle releases, a minimum waiting time of 120 seconds is observed. This interval is chosen to be at least 12 times the viscous relaxation time, denoted as $\tau = d_p^2/\nu$, noting that the specific value of the viscous time may vary across different experimental cases, resulting in a waiting time of $1 \times 10^3 \tau$. Furthermore, temperature control is critical to maintain the consistency of the experimental conditions. Therefore, the temperature of the coils is continuously monitored and held constant, with an uncertainty of $\pm 0.5°C$. Temperature control is necessary due to the influence of temperature on wire resistance.

III. SINGLE MAGNETIC SPHERE SETTLING AT FIXED ORIENTATION AND MODIFIED GRAVITY

In this Section the local gravitational pull is reduced via the magnetic gravity compensation method presented in the previous Section. It is proven that the Galileo number (and hence the settling regime) of spherical magnetic particles can be magnetically tuned. Furthermore, these results confirm the validity of the magnetic gravity compensation method. This is the first step towards the deployment of a global strategy to experimentally explore the influence of gravity in particle/fluid interactions.

A. Parameters explored

The results of an experimental study on spherical metallic particles settling in a quiescent flow at moderate Reynolds numbers performed by our group[9,10] are used here as reference data to be compared against the present measurements. Note that those experiments were performed in the water tank presented in Fig. 1 and the non-magnetic particles used had $\rho_p = 7950$ kg/m^3, which is comparable to the density of our magnetic particles.

Recall that the particles are affected in two ways due to the presence of the external magnetic inductions produced here: firstly, as the applied magnetic field is mostly vertical on the region of interest, particle rotation is partially blocked and only allowed around the vertical axis. Secondly, the spatial profile of the imposed field is specifically tailored to be as close as possible to a homogeneous vertical gradient field in the region of interest, hence particles experience an almost constant magnetic force which counteracts the gravitational force yielding different effective gravity values $\tilde{g}$.

In the sequel, the following nomenclature will be used to refer to the different experiments:

- $\varnothing B$
  Reference case with no magnetic induction[9,10].

- Case g_0
  Uniform magnetic induction (spin blocking effect). The magnetic induction profile was presented in Fig. 2(a)-(c).

- Case g^*
  Uniform magnetic induction gradient (spin blocking and modified gravity). The magnetic induction profile was presented in Fig. 2(b)-(d).

Additionally, as detailed in Section II D, the visualization area in Case g^* has a maximum adimensional height $l^*_{max} = 100$, whereas for Case g_0 $l^*_{max} = 200$. This difference is due to the finite size of the coils: it is possible to produce a homogeneous magnetic induction (Case g_0) in a larger region of space compared to the production of a homogeneous magnetic induction gradient (Case g^*).

For the Case g^*, Table III summarizes the different effective gravities $\tilde{g}$ explored (details about the estimation of $\tilde{g}$ are given in the next Subsection). The effective gravity will be given from now on in dimensionless form $g^* = \tilde{g}/g$. In practice, changing the effective gravity is simply achieved by multiplying the currents given by the optimized configuration g^* by a constant value.

TABLE III. Different magnetic induction gradients applied and regimes of effective gravity $\tilde{g}$ explored. The columns present the five different variants of the magnetic field Case g^*. The rows show the dimensionless gravities g^* defined as the ratio between the effective gravity $\tilde{g}$ and the usual gravity acceleration $g = 9.8$ m/s^2, and the values of $\nabla_z B$ evaluated at $r = 0$ (i.e. the coils' axis) previously denoted G_z.

$g^* = \tilde{g}/g$	G_z (G/m)
0.43 ± 0.02	-476 ± 42
0.65 ± 0.02	-286 ± 25
0.77 ± 0.02	-191 ± 16
0.80 ± 0.02	-171 ± 15
0.90 ± 0.02	-95 ± 8

The exploration of settling regimes is performed by independently changing the effective gravity and the fluid viscosity according to the following protocol. For a given value of fluid viscosity, all the different values of $\tilde{g}$ are applied to sweep Galileo number. In this way, with a fixed viscosity, the Galileo number can be swept by varying the effective gravity in between 65% and 100% of its value at $g = 9.8$ m/s^2. Overall, the range of Ga values explored is $[100, 280]$.

Finally, the trajectory planarity is quantified by the ratio of eigenvalues λ_2/λ_1 (with $\lambda_1 \geq \lambda_2$) of the dimensionless perpendicular (to gravity) velocity correlation matr

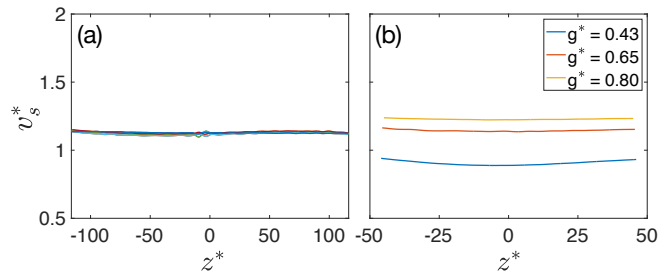### B. Terminal Velocity & Effective Gravity Homogeneity

FIG. 4. Representative settling velocities (i.e. component parallel to gravity) of spheres, versus dimensionless distance to origin, under the two external magnetic field Cases studied: g_0 and g^*. (a) Three settling velocities for Case g_0 at low Ga. (b) One settling velocity for each of the following three variants of Case g^*: $g^* = 0.43$ & Ga $= (103 \pm 5)$, $g^* = 0.65$ & Ga $= (125 \pm 5)$, and $g^* = 0.80$ & Ga $= (125 \pm 5)$.

It is important to verify that the particles reach a terminal velocity, and that there is no global deviation caused by the magnetic induction gradient inhomogeneities measured in Section II C. In this sense, Fig. 4 presents some examples of the evolution of vertical velocities versus distance to the origin (set at the geometrical center of the coils, see Section II B). Note that the figure presents single realization settling velocities while the ensemble average of tens of drops are used in all the analyses that follow.

Fig. 4(a) shows the effect of rotation blockage introduced by the magnetic induction set up of Case g_0. A terminal regime with a constant settling velocity is observed with typical variations between realizations of less than 3%. Fluctuations of this order of magnitude match those present in the non-magnetic spheres reference case. Hence the fluctuations seen in the figure are attributed to the usual variability of particles settling[9,10,36], therefore no major effect of rotation blockage is seen on the terminal velocity.

On the other hand, Fig. 4(b) shows one representative settling velocity at Ga $= (103\pm5)$, (125 ± 5), and (126 ± 5) for three dimensionless gravity values of Case g^*: $g^* = 0.43$, 0.65, and 0.80, respectively. As will be reflected in the trajectory angle discussion in what follows, the magnetic field to produce the lowest dimensionless gravity $g^* = 0.43$ is too strong and produces an horizontal drift, i.e. the perpendicular magnetic force becomes stronger than the fluid drag. In this sense, this subpanel shows that the settling velocity in that case (blue curve) is affected much more than in the other g^* cases: at $|z^*| = |z/d_p| = 46$ the velocity value increases by 8% for $g^* = 0.43$, whereas it increases less than 2% for the other cases. It is then concluded that measurements up to $g^* = 0.65$ can be expected to behave analogously to non-magnetic spheres. This claim will be confirmed in what follows and can be understood with the magnetic-to-drag radial force ratio presented in Eq. B5. That relation was computed for values of the magnetic field from Case $g^* \approx 0.65$ resulting in values lower than 10^{-3}, while the force ratio for Case $g^* \approx 0.43$ is of order 10^{-1} therefore allowing the radial magnetic force to drift particles, affecting their settling velocity.

The fact that particles reach a terminal velocity allows for the definition of a constant effective gravity, and determining its precise value is crucial. Recall the equation linking $\tilde{g}$ with the experimental parameters (see Section II A): $\tilde{g} = g - |\mathbf{M}|\nabla_z|\mathbf{B}|/m$. As previously discussed, the value of M can be computed from the manufacturer's data and $\nabla_z B$ was measured (see Subsection II C). The values of $\tilde{g}$ can then be computed.

The effective gravity can as well be obtained by measuring the terminal settling velocity with no external magnetic induction applied $v_{s,0}$ and comparing it to that of particles settling in the same flow but with its gravity being modified $v_{s,M}$. Recall that the particle settling velocity can be calculated as:

$$v_s = \sqrt{\frac{mg}{\frac{\pi}{8}C_D(Re_p)d_p^2\rho_f}}. \qquad (10)$$

The ratio $m/(\frac{\pi}{8}d_p^2\rho_f)$ is identical as the same particles are used, therefore:

$$g^* = \frac{\tilde{g}}{9.8 \ m/s^2} = \frac{v_{s,M}^2 C_D(Re_{p,M})}{v_{s,0}^2 C_D(Re_{p,0})}, \qquad (11)$$

with $Re_{p,0} = v_{s,0}d_p/\nu$, and $Re_{p,M} = v_{s,M}d_p/\nu$. Then, using usual drag correlations[9,10,44], it is possible to extract $\tilde{g}$ for all the multiples of Case g^* studied.
Values of $\tilde{g}$ that overlap with the computed ones are independently obtained from particle terminal settling velocities. Therefore the values of effective gravity $\tilde{g}$ presented in Table III are validated.

C. Path instability Results

The different path instabilities of a single spherical magnetic particle settling in a quiescent flow are presented here. The dynamics are controlled by Galileo number Ga, which varies as the square root of gravity. It is shown that by changing gravity the path instability in action can be tuned. First the trajectory angle and planarity are compared to the non-magnetic Reference Case[9,10], and, later on, the same comparison is done for trajectory oscillations.

1. Trajectories Geometry

Fig. 5 presents some representative 3D trajectories (first column) alongside a top view (second column). All these trajectories belong to Case g_0, as those of Case g^* present the same dynamics but with shorter trajectories. Each sub-panel presents results with Ga in the main four regimes previously identified:

(1) Steady Oblique – Ga = {153, 158}. Fig. 5(a) presents some trajectories in this regime. The trajectories are planar and have a well defined angle with the vertical that, after centering, form a cone in 3D space. These trajectories are *less* planar (although still overall planar) than those of Case $\emptyset B$. This difference can be observed from the planarity quantification done in the sequel (Fig. 6) where the magnetic particles have a value of $\sqrt{\lambda_2/\lambda_1} \approx 0.2$ versus 0.05 for Case $\emptyset B$[9].

(2) Oblique Oscillating – Ga = 206 (Fig. 5(b)). While trajectories at Ga = 206 would be expected to be in the Oblique Oscillating regime according to numerical simulations, non planar trajectories are observed, as represented in Fig. 5(b). The trajectories here are not planar as will be identified in the following planarity analysis. Overall these properties are similar with the trajectories belonging to the Planar or Rotating regime (Fig. 5(c)). It is likely that, considering the uncertainty in Ga, and the vicinity with the frontier to the Planar or Rotating Regime, these measurements could be attributed to the Planar or Rotating regime.

(3) Planar or Rotating – Ga = {213, 217}. Fig. 5(c) presents some trajectories in this regime. They are composed of weakly non-planar trajectories (black) and some helicoids with diameter $D \approx 10$ and pitch $P \approx 500$ (equivalent to those of Case $\emptyset B$). Note that these values are adimensionalized by the particle diameter d_p. Recall that a bi-stable region is predicted by numerical simulations and experimentally confirmed for these ranges of Ga. Apart from the effects on angle and planarity (discussed in the Case $\emptyset B$), this sub-panel makes explicit the presence of two regimes at these Ga numbers: helicoid-like trajectories coexist with oblique non-planar ones.

(4) Chaotic – Ga = 275. Finally, the Chaotic regime correctly matches the characteristics found for the Case $\emptyset B$: all trajectories are different, non-planar and oblique.

The trajectories found when the particle rotation is blocked and an effective gravity is set are indistinguishable from those found in the Reference Case of non-magnetic particles. This supports the hypothesis that rotation blockage and the addition of a magnetic force do not affect the regimes that a settling particle undergoes[37]. Furthermore, this confirms that the magnetic method to compensate gravity presented here indeed modifies gravity without any spurious effect.

2. Trajectories Angle & Planarity

Fig. 6 presents the trajectories' angle and planarity versus Ga number, alongside the reference measurements from our group[9,10] (empty circles). Additionally, the vertical dashed lines show the onsets for the different settling regimes: Rectilinear, Steady Oblique, Oblique Oscillating, Planar or Rotating, and Chaotic. In particular, Fig. 6(b) and Fig. 6(d) present the measurements against a Galileo number $Ga(\tilde{g})$ that was calculated with the effective gravity value $\tilde{g}$, whereas Fig. 6(a) and Fig. 6(c) show the measurements as a function of $Ga(g)$ number based on the actual non-perturbed gravity, i.e. $\tilde{g} = 9.8$ m/s^2. Red crosses denote the measurements from Case g_0, for which only the particle rotation is blocked and no net magnetic force modifying the effective gravity exists. The empty circles are the non-magnetic Reference Data[9], and the rest of the markers are the different configurations of Case g^* previously defined, for which effective gravity is magnetically tuned. Note that in the Reference Case $\emptyset B$ and Case g_0, the points keep the same abscissa between rows because in the Case g_0 $\tilde{g} = g = 9.8$ m/s^2.

The trajectory planarity is quantified by the ratio of eigenvalues λ_2/λ_1 (with $\lambda_1 \geq \lambda_2$) of the dimensionless perpendicular (to gravity) velocity correlation matrix defined as:

$$\langle \mathbf{v}_\perp^* \ \mathbf{v}_\perp^{*\mathrm{T}}\rangle = \begin{bmatrix} <v_x^{*2}> & <v_x^*v_y^*> \\ <v_y^*v_x^*> & <v_y^{*2}> \end{bmatrix}, \qquad (12)$$

with $v_s^* = v_s/U_g$. Perfectly planar (non-planar) trajectories yield λ_2/λ_1=0 (=1), while non-vanishing values of
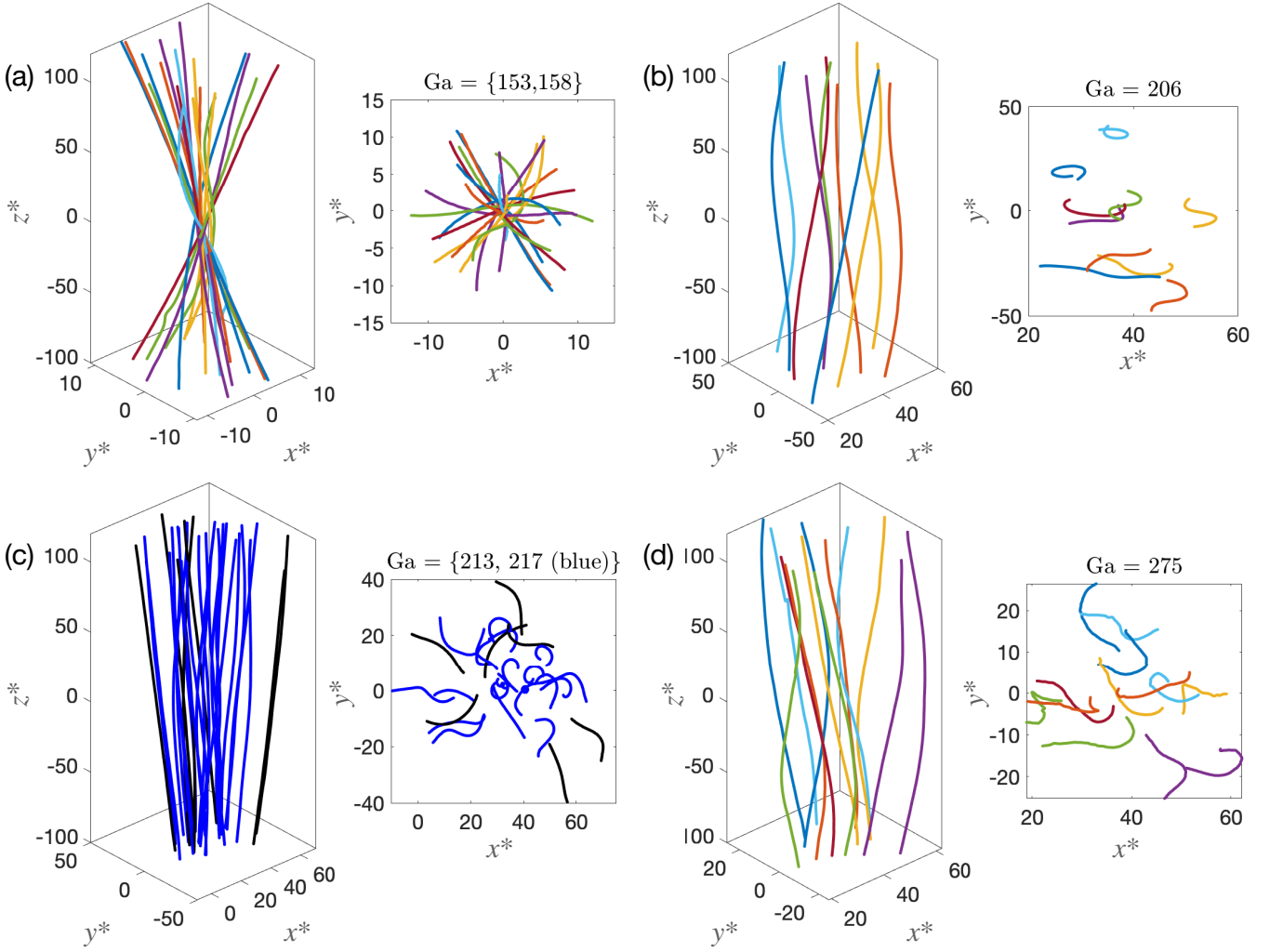
FIG. 5. Representative 3D trajectories alongside a Top View, for results with Ga in the main four regimes presented in the Introduction. Sub-panel (a) – Ga = $\{153, 158\}$, Steady Oblique regime. Sub-panel (b) – Ga = 206, Oblique Oscillating regime. Sub-panel (c) – Ga = $\{213, 217\}$, Planar or Rotating regime. Sub-panel (d) – Ga = 275, Chaotic regime. All these trajectories belong to Case g_0.

this ratio indicate a departure from planarity[37].

For both the trajectory planarity and angle, it is observed that the data points collapse into a single trend when the corrected Ga($\tilde{g}$) is used. This is consistent with the Reference Data case, including the transitions between settling regimes, whose detailed description has been reported in Cabrera-Booman et al[9]. Besides, it can be seen that the Case g_0, for which no magnetic modification to Ga is applied, presents an identical behaviour as the reference Case $\varnothing B$. The latter implies that there is no measurable effect of the particle rotation blockage on the trajectory angle or planarity. Hence, it can be inferred that the rotation blockage in the Case g^* has no major effect. On the other hand, the uniform magnetic gradient strategy indeed allows exploration of Galileo number effects and settling regimes by simply varying the amplitude of the applied field (and thus of its gradient); which

turns out to be equivalent, in terms of variations of Ga, to viscosity modifications.

Note that the single point with $\tilde{g} = (4.2 \pm 0.2)$ m/s^2 and Ga = 103 (light blue circle) that corresponds to the strongest magnetic gradient applied (Case $g^* \approx 0.43$), is off the trend in Fig. 6(c). This is due to the spurious radial magnetic force which, as already pointed out in Section III B, cannot be fully neglected for such strong effective gravity modifications. As a consequence, trajectories in this range of effective gravity acquire a small radial drift and tend to become slightly more oblique.

IV. CONCLUSIONS

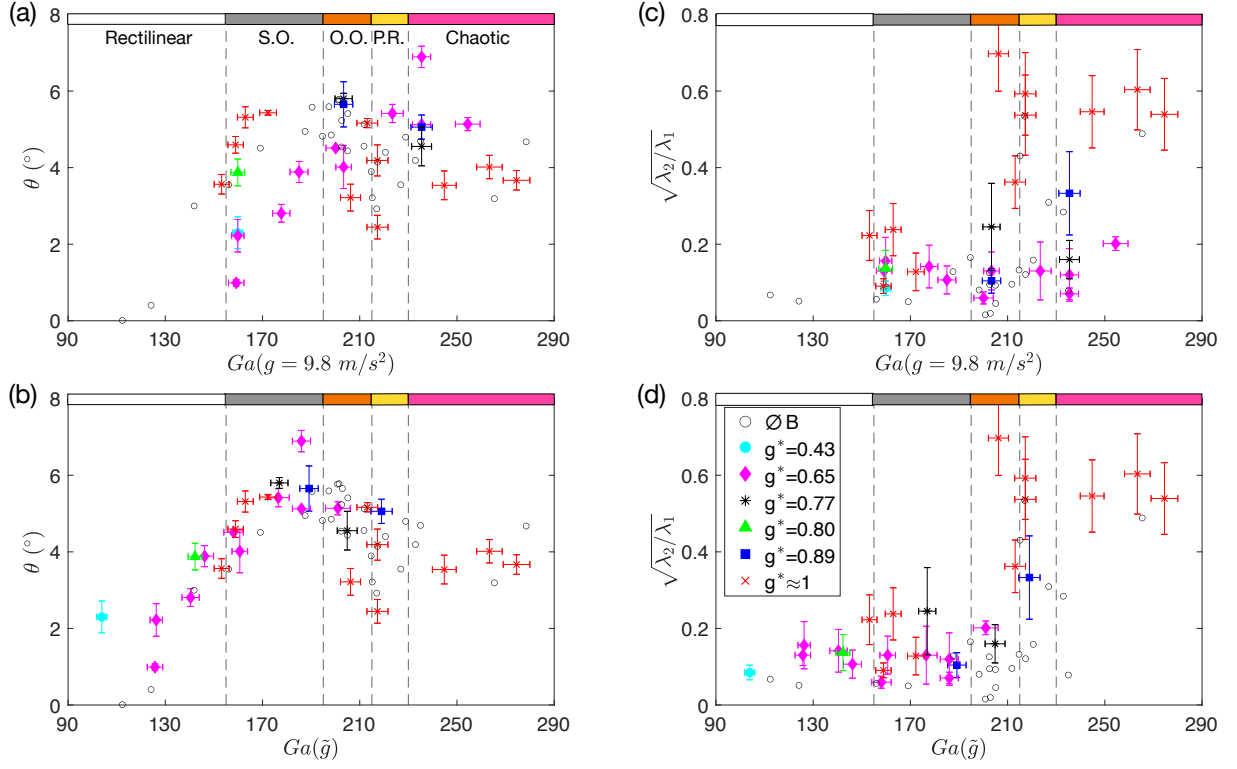This article presents both a magnetic method to modify gravity on particles in a laboratory, and experimental

FIG. 6. Trajectory angles with the vertical (a-b) and planarity (c-d) versus Ga number, alongside reference measurements (empty circles)[9,10]. Additionally, vertical dashed lines and color bars[9] show the onsets for the different regimes presented in the Introduction following the nomenclature introduced in Cabrera-Booman et al.[9]. The bottom row shows measurements against a Galileo number that was calculated with the corrected gravity value $\tilde{g}$. The top row presents measurements as a function of a Ga number computed assuming that the gravity did not change with the application of the external magnetic induction (i.e. $\tilde{g} = 9.8$ m/s^2). Finally, different markers and colors are used to distinguish the data points as denoted in the legend.

studies on the settling of single spheres in a quiescent flow with modified gravity. A magnetic method to modify gravity is developed, validated and tested. Its theoretical foundation is presented, including details on how the addition of an external magnetic induction can produce a vertical force that counteracts the gravitational force on a magnetic particle. This experimental method also blocks the perpendicular spin of magnetic particles, thus the only spin allowed is around the magnetic field direction. The homogeneity of the theoretically derived magnetic field needed to compensate gravity is detailed, showing a high level of homogeneity. The coils' positions and currents to produce the desired magnetic field are obtained from a non-linear fit, and the resulting field measured in the real world is compared to the theoretical field finding good agreement.

The settling of spherical magnets in a quiescent flow is studied and compared to a reference non-magnetic sphere settling measured by our group[9,10] as both a final validation of the method and a study of the influence of particle spinning on the particle trajectories' dynamics. The latter consists of the analysis of the dynamics of spheres in the parameter space $\Gamma - Ga$, with a particle-to-fluid density ratio $\Gamma = 8.2$ and Galileo numbers $Ga \in [100, 280]$. The terminal velocity of particles is discussed for each

effective gravity value, showing that particles achieve a homogeneous terminal velocity, thus implying that the magnetic method modifies gravity homogeneously. Trajectories in 3D that match benchmark results without gravity are shown for each regime in the path instability parameter space. The results on trajectory angle showed no difference between magnetic and non-magnetic cases thus implying that the method to compensate gravity performs well and particle spinning is not relevant for that aspect of the dynamics. On the other hand, trajectory planarity presents minimal differences in the Planar or Rotating region of the parameter space although the present measurements do not allow to conclude whether there is a rotation blockage effect.

A novel experimental method to compensate gravity on magnetic particles in a fluid has been demonstrated to compensate gravity down to a homogeneous value 6.37 m/s^2, or 65% of its full value, in the measurement volume without inducing drift or any other spurious effect on the particle dynamics. Note that this value can be further reduced by changing, for instance, the particles. Although not discussed here, this experimental technique can be minimally modified to increase the gravitational pull. There is considerable value in the method as it allows low-gravity experimentation in a laboratory bench

that otherwise would need a big budget and facilities such as parabolic flights, International Space Station or drop towers.

Appendix A: Coils' Input Parameters

The coils' positions (Z_i) and currents (I_i) given by the fit, for both cases are presented in Table IV. Note that for the Case CstB only four coils are used as that case does not require more coils to achieve better homogeneity.

TABLE IV. Coils' positions and currents given by the fit method for both Cases CstB and Cst∇_zB. The coils' names follow the nomenclature presented in Fig.1.

| | Case CstB | | Case Cst∇_zB | |
	Z (cm)	I (A)	Z (cm)	I (A)
Coil 1	✗	✗	26.5	2.28
Coil 2	14.2	4.24	24.5	-1.77
Coil 3	12	0.20	12	1.70
Coil 4	-12	0.16	0	0.52
Coil 5	-14.2	4.46	-24.5	-3.06
Coil 6	✗	✗	-26.5	-1.16

Appendix B: Gravity Compensation Theory

1. Magnetic Field Derivation

To be able to homogeneously compensate gravity, the magnetic force on gravity's direction ($\mathbf{F}^M \cdot \hat{\mathbf{z}}$) needs to be a constant independent of z here denoted G_z. Alongside the previous condition, the external magnetic field $\mathbf{B}$ has to be a solution of Maxwell's equations, leading to the following set of equations:

$$\nabla_z \ \mathrm{B} = G_z, \tag{B1}$$
$$\nabla \cdot \mathbf{B} = 0, \tag{B2}$$
$$\nabla \times \mathbf{B} = 0. \tag{B3}$$

The present work focuses on axisymmetric solutions where a linear magnetic induction in $\hat{\mathbf{z}}$ can be proposed, resulting in: $\mathbf{B}(r,z) = B_r(r) \ \hat{\mathbf{r}} + (G_z \ z + B_0) \ \hat{\mathbf{z}}$, in cylindrical coordinates. Later, B_r can be obtained by solving Eq. B2, leading to the following magnetic field induction:

$$\mathbf{B}(r,z) = (-G_z/2 \ r) \ \hat{\mathbf{r}} + (G_z \ z + B_0) \ \hat{\mathbf{z}}.$$

This magnetic induction respects the irrotational condition (Eq. B3), whereas Eq. B1 is only exactly satisfied at $r = 0$. The latter is an unavoidable consequence of the solenoidal nature of magnetic fields. A dependence on the distance to the system axis (r) and the position on the axis (z) are then present in the forces acting on
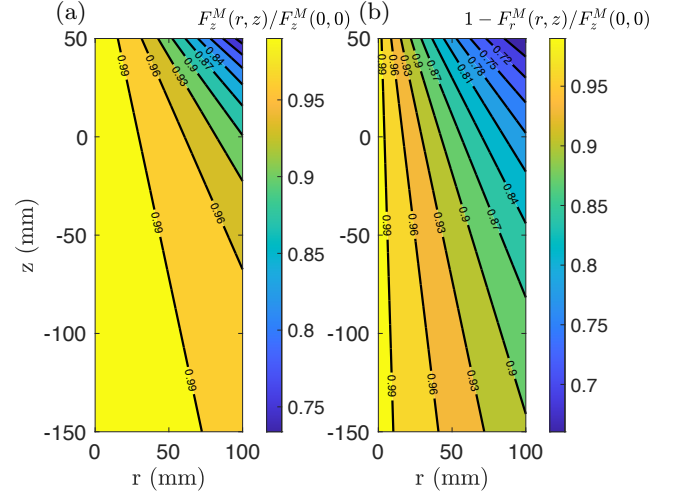

FIG. 7. Contour plot of the axial (a) and radial (b) component of the theoretical magnetic force, normalised by the axial force at z=0: $F_z^M(r,z)/F_z^M(0,0)$ and 1-$F_r^M(r,z)/F_z^M(0,0)$, respectively.

the particle:

$$F_z^M(r,z) = M \ \frac{\partial B}{\partial z} = M \ \frac{(G_z z + B_0)G_z}{\sqrt{(G_z/2)^2/4r^2 + (G_z z + B_0)^2}},$$
$$F_r^M(r,z) = M \ \frac{\partial B}{\partial r} = M \ \frac{r \ (G_z)^2/4}{\sqrt{(G_z)^2/4r^2 + (G_z z + B_0)^2}}. \tag{B4}$$

Note that $F_r^M(r \to 0) = 0$ and $F_z^M(r \to 0) = MG_z$. Therefore, gravity can be fully compensated at $r = 0$, without any radial force present. Note that this is not in conflict with Earnshaw's theorem[11] because the equilibrium is not stable, i.e. the Laplacian of the magnetic energy is not zero.

2. Magnetic Field Homogeneity

Fig. 7 presents contour plots of $F_z^M(r,z)/F_z^M(0,0)$ and 1-$F_r^M(r,z)/F_z^M(0,0)$, note that the normalization chosen is $F_z^M(0,0) = MG_z$. Values of $G_z = -250$ G/m, $B_0 = 26$ G, $z \in (-150, 50)$ mm and $M = 4.96 \times 10^{-8}$ G^{-1}m^{2}s^{-2} were used to compute the forces from Equations B4, as these are typical magnitudes for the present experimental setup.

The axial component of the force F_z^M has a weak dependence on z and r, as quantified in Fig. 7(a): a maximum axial force variation of 20% is achieved at $z = 50$ mm and $r = 100$ mm. At $z \in (-150,0)$ mm and $r \in (0,20)$ mm, the ranges used in this work, the axial magnetic force has fluctuations below 2%. On the other hand, the radial force F_r^M has a stronger dependence on r and z (see Fig.7(b)). When $r = 100$ mm and $z = 50$, the radial force becomes as high as 30% of the reference axial force at the center $F_z^M(0,0)$. At the ranges $z \in (-150,0)$ mm

and $r \in (0, 50)$ mm the maximum value of radial force is reduced to 10% of its axial counterpart.

On the other hand, the relative magnitude of the axial and radial forces can be calculated:

$$\frac{F_r^M(r,z)}{F_z^M(r,z)} = \frac{1}{4}\frac{G_z \, r}{G_z \, z + B_0}. \tag{B5}$$

As the aspiration is to solely counteract gravity, a radial force is not desired and the latter ratio needs to be minimized. There are two ways to achieve it: keep r small compared to $(z + B_0/G_z)$; and/or have the largest possible value for B_0. The latter approach is ideal because it allows a larger volume (r-z) where the axial force is homogeneous and the radial forces are small. Albeit it translates to more current on the coils (recall that $B \propto I$) and, therefore, thicker coils winding that might lead to the necessity of external cooling.

3. Equations of Motion

When applying this method to a particle in a fluid the equations of motion need to include hydrodynamical effects. Neglecting added mass and history forces[45,46], the fluid adds drag[44], torque[47] and buoyancy effects yielding the following equations of motion:

$$\mathbf{F} = (m_p - V\rho_f)g \, \hat{\mathbf{z}} - \mathbf{M} \cdot \nabla\mathbf{B} - \frac{1}{8}C_D\pi d_p^2\rho_f\mathbf{v}|\mathbf{v}|, \tag{B6}$$

$$\mathbf{T} = -1/64 C_\omega\rho_f\boldsymbol{\omega}|\boldsymbol{\omega}|d_p^5 - \mathbf{M} \times \mathbf{B}, \tag{B7}$$

with fluid density ρ_f and particle volume V, kinematic viscosity ν, translational (C_D) and rotational (C_ω) drag coefficients, particle velocity $\mathbf{v}$, and angular velocity $\boldsymbol{\omega}$. Finally, note that if the Reynolds number is low (typically below order one[48], i.e. the Stokes regime) the fluid drag and torque are simpler:

$$\mathbf{F} = (m_p - V\rho_f)g \, \hat{\mathbf{z}} - \nabla(\mathbf{M} \cdot \mathbf{B}) - 3\pi d_p\eta\mathbf{v}, \tag{B8}$$

$$\mathbf{T} = \pi\eta d_p^3\omega - \mathbf{M} \times \mathbf{B}. \tag{B9}$$

Appendix C: Particle Material Discussion

Equation 1 can be rewritten if one specifies the particle magnetic properties: in the ferromagnetic, paramagnetic, or diamagnetic particle cases $\mathbf{M} \propto \mathbf{B}$; whereas for a permanent magnet (with $B = |\mathbf{B}|$ below its coercive field strength) $M = |\mathbf{M}|$ is constant and $\mathbf{F}^M = \mathbf{M} \cdot \nabla\mathbf{B}$. This work focuses on the latter particle case as magnetic moment values are at least two orders of magnitude larger. This translates into lower external magnetic induction intensities (i.e. less power or smaller coils) to achieve a certain magnetic force.

In particular, the magnetic moment M of a permanent magnet can be computed, if one assumes that the magnetic dipolar moment is dominant, in the following manner:

$$M = \frac{B_{\mathrm{res}}V}{\mu_0}, \tag{C1}$$

where V is the volume of the magnet, μ_0 the vacuum magnetic permeability (note that $\mu_0 \approx \mu_{\mathrm{water}}$) and B_{res} is the remnant magnetic flux density (for the particles here used $B_{\mathrm{res}} = 1.192$ T), in other words the magnet's magnetic flux density when the external coercive field strength is zero.

REFERENCES

[1] Karl Cardin, Christophe Josserand, and Raúl Bayoán Cal. Droplet capture in a fiber array. *Phys. Rev. Fluids*, 8:043601, Apr 2023.

[2] W. Hwang and J.K. Eaton. Turbulence attenuation by small particles in the absence of gravity. *International Journal of Multiphase Flow*, 32(12):1386–1396, 2006.

[3] T Fallon and C B Rogers. Turbulence-induced preferential concentration of solid particles in microgravity conditions. *Experiments in Fluids*, 33(2):233–241, 2002.

[4] Karl Cardin, Facundo Cabrera-Booman, and Raúl Bayoán Cal. Droplet jump from a particle bed, 2023.

[5] M. Horowitz and C. H. K. Williamson. The effect of reynolds number on the dynamics and wakes of freely rising and falling spheres. *Journal of Fluid Mechanics*, 651:251–294, 2010.

[6] C.H.J. Veldhuis and A. Biesheuvel. An experimental study of the regimes of motion of spheres falling or ascending freely in a newtonian fluid. *International journal of multiphase flow*, 33(10):1074–1087, 2007.

[7] G. Bouchet, M. Mebarek, and J. Dušek. Hydrodynamic forces acting on a rigid fixed sphere in early transitional regimes. *European Journal of Mechanics - B/Fluids*, 25(3):321–336, 2006.

[8] W. Zhou and J. Dusek. Chaotic states and order in the chaos of the paths of freely falling and ascending spheres. *International Journal of Multiphase Flow*, 75:205–223, 2015.

[9] Facundo Cabrera-Booman, Nicolas Plihon, and Mickaël Bourgoin. Path instabilities and drag in the settling of single spheres, 2023.

[10] F. Cabrera. *Settling of particles in quiescent and turbulent flows. From ground conditions to micro-gravity*. PhD thesis, École Normale Supérieure de Lyon, 2021.

[11] Earnshaw. *S. Trans. Camb. Phil. Soc.*, page 97–112.

[12] E Beaugnon and R Tournier. Levitation of organic materials. *Nature*, 349(6309):470, 1991.

[13] M. D. Simon and A. K. Geim. Diamagnetic levitation: Flying frogs and floating magnets (invited). *Journal of Applied Physics*, 87(9):6200–6204, 2000.

[14] Magnetic separation techniques in sample preparation for biological analysis: A review. *Journal of Pharmaceutical and Biomedical Analysis*, 101:84–101, 2014. JPBA Reviews 2014.

[15] H. Okada, H. Okuyama, M. Uda, and N. Hirota. Removal of aerosol by magnetic separation. *IEEE Transactions on Applied Superconductivity*, 16(2):1084–1087, 2006.

[16] Separation of mixed waste plastics via magnetic levitation. *Waste Management*, 76:46–54, 2018.

[17] Gradient coil design: A review of methods. *Magnetic Resonance Imaging*, 11(7):903–920, 1993.

[18] S.S. Hidalgo-Tobon. Theory of gradient coil design methods for magnetic resonance imaging. *Concepts in Magnetic Resonance Part A*, 36A(4):223–242.

[19] Jun-Hua Pan, Nian-Mei Zhang, and Ming-Jiu Ni. Instability and transition of a vertical ascension or fall of a free sphere affected by a vertical magnetic field. *Journal of Fluid Mechanics*, 859:33–48, 2019.

[20] Mailfert, Alain, Beysens, Daniel, Chatain, Denis, and Lorin, Clément. Magnetic compensation of gravity in fluids: performance and constraints. *Eur. Phys. J. Appl. Phys.*, 71(1):10902, 2015.

[21] D Chatain, D Beysens, K Madet, V Nikolayev, and A Mailfert. Study of fluid behaviour under gravity compensated by a magnetic field. *Microgravity - Science and Technology*, (3):196–199.

[22] Clément Lorin, Alain Mailfert, Christian Jeandey, and Philippe J. Masson. Perfect magnetic compensation of gravity along a vertical axis. *Journal of Applied Physics*, 113(14):143909, 2013.

[23] V S Nikolayev, D Chatain, D Beysens, and G Pichavant. Magnetic Gravity Compensation. *Microgravity Science and Technology*, 23(2):113–122, 2011.

[24] F Box, E Han, C R Tipton, and T Mullin. On the motion of linked spheres in a Stokes flow. *Experiments in Fluids*, 58(4):29, 2017.

[25] Jérémy Vessaire, Nicolas Plihon, Romain Volk, and Mickaël Bourgoin. Sedimentation of a suspension of paramagnetic particles in an external magnetic field. *Phys. Rev. E*, 102:023101, Aug 2020.

[26] Eric E. Keaveny and Martin R. Maxey. Spiral swimming of an artificial micro-swimmer. *Journal of Fluid Mechanics*, 598:293–319, 2008.

[27] V. Kumaran. Rheology of a suspension of conducting particles in a magnetic field. *Journal of Fluid Mechanics*, 871:139–185, 2019.

[28] H. M. De La Rosa Zambrano, G. Verhille, and P. Le Gal. Fragmentation of magnetic particle aggregates in turbulence. *Phys. Rev.s Fluids*, 3:084605, Aug 2018.

[29] Luca Brandt and Filippo Coletti. Particle-Laden Turbulence: Progress and Perspectives. *Annual Review of Fluid Mechanics*, 54(1):159–189, 2022.

[30] C. M. Tchen. *Mean value and correlation problems connected with the motion of small particles suspended in a turbulent fluid*. PhD thesis, TU Delft, 1947.

[31] Kyle D. Squires and John K. Eaton. Preferential concentration of particles by turbulence. *Physics of Fluids A: Fluid Dynamics*, 3(5):1169–1178, 1991.

[32] F. Falkinhoff, M. Obligado, M. Bourgoin, and P. D. Mininni. Preferential concentration of free-falling heavy particles in turbulence. *Phys. Rev. Lett.*, 125:064504, Aug 2020.

[33] Shravan K.R. Raaghav, Christian Poelma, and Wim-Paul Breugem. Path instabilities of a freely rising or falling sphere. *International Journal of Multiphase Flow*, 153:104111, 2022.

[34] Mathieu Jenny, Gilles Bouchet, and Jan Dusek. Nonvertical ascension or fall of a free sphere in a newtonian fluid. *Physics of Fluids*, 15(1):L9–L12, 2003.

[35] M. Jenny, J. Dusek, and G. Bouchet. Instabilities and transition of a sphere falling or ascending freely in a newtonian fluid. *Journal of Fluid Mechanics*, 508:201–239, 2004.

[36] O. J. I. Kramer, P. J. de Moel, S. K. R. Raaghav, E. T. Baars, W. H. van Vugt, W.-P. Breugem, J. T. Padding, and J. P. van der Hoek. Can terminal settling velocity and drag of natural particles in water ever be predicted accurately? *Drinking Water Engineering and Science*, 14(1):53–71, 2021.

[37] Wei Zhou. *Instabilités de trajectoires de spheres, ellipsoides et bulles*. PhD thesis, 2016.

[38] R.P Chhabra, S Agarwal, and K Chaudhary. A note on wall effect on the terminal falling velocity of a sphere in quiescent newtonian media in cylindrical tubes. *Powder Technology*, 129(1):53–58, 2003.

[39] M. Bourgoin and S. G. Huisman. Using ray-traversal for 3d particle matching in the context of particle tracking velocimetry in fluid mechanics. *Rev. Sci. Instr.*, 91(8):085105, 2020.

[40] Roger I. Tanner and Shaocong Dai. Particle roughness and rheology in noncolloidal suspensions. *Journal of Rheology*, 60(4):809–818, 2016.

[41] Yu Zhao and Robert H. Davis. Interaction of sedimenting spheres with multiple surface roughness scales. *Journal of Fluid Mechanics*, 492:101–129, 2003.

[42] Indresh Rampall, Jeffrey R. Smart, and David T. Lighton. The influence of surface roughness on the particle-pair distribution function of dilute suspensions of non-colloidal spheres in simple shear flow. *Journal of Fluid Mechanics*, 339:1–24, 1997.

[43] Nicholas T Ouellette, Haitao Xu, and Eberhard Bodenschatz. A quantitaive study of three-dimensional Lagrangian particle tracking algorithms. *Experiments in Fluids*, 39:722, 2005.

[44] Phillip P. Brown and Desmond F. Lawler. Sphere drag and settling velocity revisited. *Journal of Environmental Engineering*, 129(3):222–231, 2003.

[45] R. Gatignol. The faxén formulae for a rigid particle in an unsteady non-uniform stokes flow. *J. Méc. Theor. Appl.*, 1(143), 1983.

[46] Martin R. Maxey and James J. Riley. Equation of motion for a small rigid sphere in a nonuniform flow. *The Physics of Fluids*, 26(4):883–889, 1983.

[47] Nikolay Lukerchenko, Yury Kvurt, Alexander Kharlamov, Zdenek Chara, and Pavel Vlasak. Experimental evaluation of the drag force and drag torque acting on a rotating spherical particle moving in fluid. *Journal of Hydrology and Hydromechanics*, 56:88–94, 01 2008.

[48] F. Cabrera, M. Z. Sheikh, B. Mehlig, N. Plihon, M. Bourgoin, A. Pumir, and A. Naso. Experimental validation of fluid inertia models for a cylinder settling in a quiescent flow. *Phys. Rev. Fluids*, 7:024301, Feb 2022.